

## DISPERSAL OF PROTOPLANETARY DISKS BY CENTRAL WIND STRIPPING

I. MATSUYAMA<sup>1</sup>

Department of Earth and Planetary Science, University of California, Berkeley, 307 McCone Hall, Berkeley, CA 94720, USA

D. JOHNSTONE<sup>2</sup>

National Research Council of Canada, Herzberg Institute of Astrophysics, 5071 West Saanich Road, Victoria, BC V9E 2E7, Canada

AND

D. HOLLENBACH<sup>3</sup>

SETI Institute, 515 N. Whisman Road, Mountain View, CA 94043, USA

*Draft version August 10, 2021*

### ABSTRACT

We present a model for the dispersal of protoplanetary disks by winds from either the central star or the inner disk. These winds obliquely strike the flaring disk surface and strip away disk material by entraining it in an outward radial-moving flow at the wind-disk interface which lies several disk scale heights above the mid-plane. The disk dispersal time depends on the entrainment velocity,  $v_d = \epsilon c_s$ , at which disk material flows into this turbulent shear layer interface, where  $\epsilon$  is a scale factor and  $c_s$  is the local sound speed in the disk surface just below the entrainment layer. If  $\epsilon \sim 0.1$ , a likely upper limit, the dispersal time at 1 AU is  $\sim 6$  Myr for a disk with a surface density of  $10^3$  g cm<sup>-2</sup>, a solar mass central star, and a wind with an outflow rate  $\dot{M}_w = 10^{-8} M_\odot \text{ yr}^{-1}$  and terminal velocity  $v_w = 200$  km s<sup>-1</sup>. When compared to photoevaporation and viscous evolution, wind stripping can be a dominant mechanism only for the combination of low accretion rates ( $\lesssim 10^{-8} M_\odot \text{ yr}^{-1}$ ) and wind outflow rates approaching these accretion rates. This case is unusual since generally outflow rates are  $\lesssim 0.1$  of accretion rates.

*Subject headings:* planetary systems: protoplanetary disks — stars: winds, outflows — hydrodynamics — accretion, accretion disks

### 1. INTRODUCTION

A crucial timescale in planet formation is the timescale required for the loss of protoplanetary gas material which initially dominates the total disk mass. The outcome for a particular planetary system might be very different if the parent disk is dispersed faster or slower than in our solar system. However, relatively little attention has been paid to the processes responsible for dispersing protoplanetary disks. Hollenbach et al. (1994) set a theoretical framework and Shu et al. (1993) applied it to propose photoevaporation of the solar nebula as the disk dispersal mechanism capable of explaining the differences in envelope masses between the gas-rich giants, Jupiter and Saturn, and the gas-poor giants, Uranus and Neptune. Hollenbach et al. (2000) generalized the discussion, describing the variety of possible disk dispersal mechanisms. The dominant disk dispersal mechanism at the inner parts of the disk is viscous accretion onto the central star. However, this process becomes inefficient with time as the outer disk continuously expands to conserve angular momentum and the accretion rate decreases. Other possible disk dispersal mechanisms are planet formation, stellar encounters, stellar winds or disk winds, and photoevaporation by energetic photons. Photoevaporation is a process in which the surface of the disk is heated by stellar photons, resulting in a hydrodynamical flow, a slow wind ( $\lesssim 10$  km s<sup>-1</sup>), back to the interstellar medium. Hollenbach et al. (2000) concluded that planet formation is a minor disk dispersal mechanism, and that the dominant mechanisms for a wide range of disk sizes are viscous accretion in the inner disk and photoevaporation in the outer disk. Therefore, planet formation must compete with these more efficient dispersal mechanisms.

Handbury & Williams (1976) found that a stellar wind could not have removed the solar nebula. They argue that the stellar wind could only push the nebula to a finite distance determined by force balance and angular momentum conservation. However, they assumed that the stellar wind pushes the nebula as a whole and that the nebula maintains Keplerian rotation. Yun et al. (2007) studied the geometrical and thermal structure of the wind-disk interface for the specific case of a passive disk. However, they did not consider disk dispersal by wind stripping. Cameron (1973) suggested that the interaction of an outflowing stellar wind with the solar nebula would lead to significant mass loss, and Horedt (1978) and Elmegreen (1978) proposed models which did consider disk dispersal. Although both of these models predict significant mass loss, the manner in which the disk is dispersed is remarkably different. Horedt (1978)

Electronic address: isa@berkeley.edu

<sup>1</sup> Department of Terrestrial Magnetism, Carnegie Institution of Washington, 5241 Broad Branch Road NW, Washington, DC 20015

<sup>2</sup> Department of Physics and Astronomy, University of Victoria, Victoria, BC V8P 1A1, Canada

<sup>3</sup> NASA Ames Research Center, Mail Stop 245-6, Moffett Field, CA 94035, USA

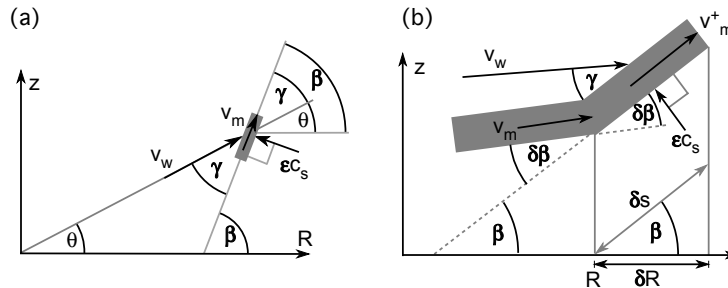


FIG. 1.— (a) Mass flow from the wind (with velocity  $v_w$  and incidence angle  $\gamma$ ) and the underlying disk (with velocity  $\epsilon c_s$  perpendicular to the mixing layer surface) to the wind-disk mixing layer. There is mass transport through the mixing layer in the direction of the local tangent angle,  $\beta$ , at velocity  $v_m$ . (b) A mixing layer annulus of length  $\delta s$  between  $R$  and  $R + \delta R$  receives mass, momentum, and angular momentum from the wind (with velocity  $v_w$  and incidence angle  $\gamma$ ), the disk (with velocity  $\epsilon c_s$  perpendicular to the mixing layer surface), and the inner annulus (with velocity  $v_m$  and incidence angle  $\delta\beta$ ), while it delivers mass and momentum to the outer annulus (with velocity  $v_m^+$ ). The local tangent of the mixing layer surface is given by  $dz/dR = \tan \beta$ .

predicts that the wind drives an outward flow, while Elmegreen (1978) predicts, somewhat paradoxically, that the wind ultimately drives an inward flow. The difference between these two models is discussed in Elmegreen (1979). In particular, the wind-disk interface is given a priori in Horedt (1978), while it is calculated in Elmegreen (1978) by considering normal pressure balance. We follow the latter course here. Elmegreen (1978) showed that if the momentum is deposited where the wind strikes the disk, the addition of low angular momentum wind material causes the underlying layers to spiral inwards. As we will show below, if Keplerian rotation is assumed in the mixing layer, the net radial flow is inward. In this case, the wind causes disk dispersal by accelerating accretion onto the central star, as shown by Elmegreen (1978).

We consider the alternative case of a shear mixing layer whose rotation is non-Keplerian but conserves momentum of wind and entrained disk surface material. The velocity shear is large and the tenuous surface material moves outward at speeds greater than the gravitational escape speeds. The disk material is expected to be entrained into the wind-disk interface in this case, and is carried outwards to the interstellar medium. The entrainment layer, or shear layer, carries with it a mixture of shocked wind material as well as entrained disk material.

The observationally inferred wind mass loss rate in T Tauri stars can be as high as  $\sim 10^{-7} M_\odot \text{ yr}^{-1}$  (e.g. Cabrit et al. 1990; Hartigan et al. 1995; White & Hillenbrand 2004). For comparison, the present mass loss rate of the Sun’s stellar wind is  $\sim 10^{-14} M_\odot \text{ yr}^{-1}$ . The strong magnetic activity in young stars is capable of driving stellar winds with outflow rates  $\lesssim 10^{-8} M_\odot \text{ yr}^{-1}$  (Decampli 1981). In young stars with accretion disks, the interaction of the rotating magnetic field with the accreting disk can generate outflows with mass loss rates  $\lesssim 10^{-7} M_\odot \text{ yr}^{-1}$  for correspondingly high accretion rates  $\lesssim 10^{-6} M_\odot \text{ yr}^{-1}$  (see review by Koenigl & Ruden 1993). It remains unclear whether the outflows are launched near the magnetospheric truncation radius (Shu et al. 2000) or over a wider range in disk radii (Koenigl & Pudritz 2000). Our emphasis here is on the subsequent interaction of the wind, however launched, with the protoplanetary disk. Thus, hereafter we will simply refer to the stellar wind or the disk outflow as the central wind.

The rest of the paper is organized as follows. §2 describes the theory, which incorporates pressure balance; and mass, momentum, and angular momentum conservation. §3 presents the results of applying the theory to protoplanetary disks. Finally, §4 summarizes the main results and discusses some of their consequences.

## 2. MODEL

### 2.1. Wind-disk mixing layer

Following the analysis of Hollenbach et al. (2000), we assume that disk dispersal by the stellar wind occurs in a thin mixing layer at height  $z(R)$ , where  $R$  is the disk radius. Disk material flows into this mixing layer with speed  $\epsilon c_s$ , where  $c_s$  is the sound speed and  $\epsilon$  is the entrainment efficiency, as shown in Figure 1. This type of model has been applied to protostellar jets entraining circumstellar material by Canto & Raga (1991). Since the disk cannot react to changes at velocities faster than the sound speed,  $\epsilon = 1$  is a natural upper limit to the possible value of the entrainment efficiency. Experimental results at high Mach numbers in the regime that is relevant for central winds suggest that  $\epsilon \sim 0.1$  is a more likely upper limit (Canto & Raga 1991). We will consider entrainment efficiencies in the range 0.01 – 1.

We denote the wind density, velocity, and incidence angle as  $\rho_w$ ,  $v_w$ , and  $\gamma$  respectively; the disk density and Keplerian angular velocity as  $\rho_d$  and  $\Omega_k$ ; and the mixing layer surface density, velocity, inclination, and angular velocity as  $\Sigma_m$ ,  $v_m$ ,  $\beta$ , and  $\Omega_m$  respectively. The wind incidence angle,  $\gamma$ , and the mixing layer inclination,  $\beta$ , are related by

$$\beta = \gamma + \theta, \quad (1)$$

where  $\tan \theta = z/R$  (Figure 1).

In Appendix A, we derive equations for pressure balance, and mass, momentum, and angular momentum conservation in the mixing layer. For the benefit of the reader, we repeat these equations here:

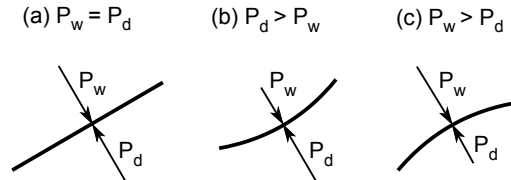


FIG. 2.— Relationship between the curvature of the mixing layer and normal pressure balance given by equation (2). The wind pressure is given by  $P_w \equiv \rho_w v_w^2 \sin^2 \gamma$  and the total disk pressure is given by  $P_d = \rho_d c_s^2 (1 + \epsilon^2)$ .

$$0 = \rho_w v_w^2 \sin^2 \gamma - \rho_d c_s^2 (1 + \epsilon^2) + \Sigma_m v_m^2 \cos \beta \frac{\partial \beta}{\partial R} \quad (2)$$

$$\frac{\partial \Sigma_m}{\partial t} = \rho_w v_w \sin \gamma + \rho_d \epsilon c_s - \frac{\cos \beta}{R} \frac{\partial}{\partial R} (R \Sigma_m v_m) \quad (3)$$

$$\frac{\partial}{\partial t} (\Sigma_m v_m) = \rho_w v_w^2 \sin \gamma \cos \gamma - \frac{\cos \beta}{R} \frac{\partial}{\partial R} (R \Sigma_m v_m^2) \quad (4)$$

$$\frac{\partial}{\partial t} (\Sigma_m \Omega_m) = \rho_d \epsilon c_s \Omega_k - \frac{\cos \beta}{R^3} \frac{\partial}{\partial R} (R^3 \Sigma_m v_m \Omega_m). \quad (5)$$

Equation (2) describes normal pressure balance in the mixing layer. On the right-hand-side (RHS) of this equation, the first and second terms correspond to the normal pressures of the wind and the disk respectively, while the third term describes the centrifugal force associated with the mixing layer curvature. A similar, so-called centrifugal correction, term has been considered in previous studies (Hayes & Probst 1966, p. 137, eq. 3.2.7; Canto 1980, eq. 10; Hartmann & Raymond 1989, eq. 7b; Wilkin & Stahler 1998, eq. 34). While these studies assume that the tangential momentum of the mixing layer is given by the total accumulated tangential momentum of the wind, we calculate it self-consistently by solving for  $\Sigma_m$ ,  $v_m$ , and  $\beta$  from equations (2)-(5).

Figure 2 illustrates the relationship between the mixing layer curvature and normal pressure balance given by equation (2). If the wind pressure,  $\rho_w v_w^2 \sin^2 \gamma$ , is equal to the total disk pressure,  $\rho_d c_s^2 (1 + \epsilon^2)$ , the curvature,  $\cos \beta \partial \beta / \partial R$ , is zero, as shown in Figure 2a. If the total disk pressure is larger than the wind pressure, the curvature is positive and the mixing layer becomes concave on the side of the wind (i.e. the mixing layer surface flares outward with increasing radius), as shown in Figure 2b. Conversely, if the wind pressure is larger than the total disk pressure, the curvature is negative and the mixing layer becomes concave on the side of the disk, as shown in Figure 2c.

Equation (3) describes mass conservation. At a given radius, disk material mixes not only with the wind but also with the wind material already mixed with the disk gas at smaller radii. On the RHS of this equation, the first and second terms describe mass input from the wind and the disk respectively, and the third term describes mass transport through the mixing layer. If we ignore the wind and disk mass input, equation (3) is similar to the standard continuity equation in cylindrical coordinates,

$$\frac{\partial \Sigma_m}{\partial t} + \frac{1}{R} \frac{\partial}{\partial R} (\Sigma_m R v_m) = 0. \quad (6)$$

The factor of  $\cos \beta$  in our continuity equation (3) arises because of the non-zero, variable, inclination of the mixing layer. Note that if we ignore the wind and disk contributions, equations (3) and (6) are equivalent for  $\beta = 0$ , as expected.

Equation (4) describes tangential momentum conservation. The first and second terms on the RHS of this equation correspond to the wind contribution and the tangential momentum transport through the mixing layer respectively. Once again, the factor of  $\cos \beta$  arises because of the non-zero, variable, inclination of the mixing layer.

Equation (5) describes angular momentum conservation. The first term on the RHS of this equation corresponds to the angular momentum contribution from the underlying disk, while the second term describes the angular momentum flux through the mixing layer. We assume that the central wind does not carry appreciable angular momentum.

Combining equations (3) and (5) yields

$$v_m = \frac{R^2 [\rho_d \epsilon c_s (\Omega_k - \Omega_m) - \Sigma_m \partial_t \Omega_m - \Omega_m \rho_w v_w \sin \gamma]}{\Sigma_m \cos \beta \partial_R (\Omega_m R^2)}. \quad (7)$$

If we assume Keplerian rotation for the mixing layer ( $\Omega_m = \Omega_k$  and  $\partial_t \Omega_m = 0$ ), equation (7) shows that the mass flow must be toward the central star ( $v_m < 0$ ), which is essentially in agreement with the result of Elmegreen (1978). As we will show in the next section, outward flow is possible if we relax the assumption of Keplerian rotation in the shearing mixing layer at the interface of wind and disk.

We can write the disk mass loss rate per unit time and disk gas surface area as

$$\dot{\Sigma}_{ws} = \frac{2 \rho_d \epsilon c_s}{\cos \beta}, \quad (8)$$

where the factor of two accounts for mass loss from both sides of the disk and the factor of  $\cos \beta$  accounts for the

inclination of the mixing layer. The characteristic dispersal time at a given radius due to mass loss to the mixing layer can be written as

$$t_{ws} \equiv \frac{\Sigma_d}{\dot{\Sigma}_{ws}} = \frac{\Sigma_d \cos \beta}{2\rho_d \epsilon c_s}. \quad (9)$$

### 2.2. Disk

We assume hydrostatic equilibrium in the vertical direction to write the disk density as

$$\rho_d(R, z) = \frac{\Sigma_d \exp[-z^2/(2H^2)]}{\sqrt{2\pi} H \text{erf}[z_m/\sqrt{2}H]} \quad (10)$$

for  $z < z_m$ , where  $\Sigma_d$  is the gas surface density of the disk,  $z_m$  is the mixing layer height,  $\text{erf}(x)$  is the error function, and  $H$  is the disk scale height. The disk scale height is given by

$$H(R) \equiv R \left( \frac{k_B T_d R}{GM_* \mu} \right)^{1/2}, \quad (11)$$

where  $k_B$  is Boltzmann's constant,  $T_d$  is the disk temperature at radius  $R$ ,  $\mu = 2.34 m_H$  is the disk mean particle mass, and  $m_H$  is the mass of a hydrogen atom. For a thin flat disk,  $T_d \propto R^{-3/4}$ , while for a disk that flares outward (Eq. 11), a larger fraction of the stellar flux is intercepted and  $T_d \propto R^{-1/2}$  (Kenyon & Hartmann 1987). We assume a midplane disk temperature power law distribution,  $T_d = 100 \text{ K}(R/\text{AU})^{-1/2}$  (D'Alessio et al. 1998).

In the so-called “ $\alpha$ -disk” theory (Shakura & Sunyaev 1973), the viscosity,  $\nu$ , is parameterized as  $\nu = \alpha c_s H$ , where  $\alpha$  is a dimensionless constant parameter. For our adopted disk temperature profile, viscous diffusion causes the surface density profile to approach  $\Sigma_d \propto R^{-1}$ , regardless of specific initial conditions (Lynden-Bell & Pringle 1974; Hartmann et al. 1998). We adopt a power-law for the radial dependence of the disk gas surface density,

$$\Sigma_d(R) = 10^3 \text{ g cm}^{-2} \left( \frac{R}{\text{AU}} \right)^{-1}. \quad (12)$$

The characteristic viscous evolution time scale is given by

$$t_\nu \sim \frac{R^2}{\nu} \sim 0.4 \text{ Myr} \left( \frac{R}{\text{AU}} \right) \left( \frac{\alpha}{10^{-3}} \right)^{-1}. \quad (13)$$

Comparison of predictions from similarity solutions with observed accretion rates and disk sizes suggests  $\alpha \sim 10^{-2}$  (Hartmann et al. 1998), while the observed semimajor axis distribution of extrasolar planets suggests  $\alpha \sim 10^{-4}$  (Ida & Lin 2005). We will consider  $\alpha$  values in this range.

The accretion rate can be written as

$$\dot{M}_{acc} = 3\pi\nu\Sigma_d \sim 3 \times 10^{-8} \text{ M}_\odot \text{ yr}^{-1} \left( \frac{\alpha}{10^{-2}} \right) \left( \frac{\Sigma_0}{10^3 \text{ g cm}^{-2}} \right) \left( \frac{T_0}{100 \text{ K}} \right) \left( \frac{M_*}{1 \text{ M}_\odot} \right)^{-1/2}, \quad (14)$$

where  $\Sigma_0$  and  $T_0$  are the surface density and disk temperature at 1 AU. The radial velocity of the accretion flow is  $\sim 2 \text{ cm s}^{-1}(\alpha/10^{-3})$ . Hence our assumption that only material and not radial momentum crosses into the mixing layer.

The inner boundary is chosen such that the wind velocity is equal to the escape velocity from the star at this radius:

$$R_{min} = \frac{2GM_*}{v_w^2} \sim 0.2 \text{ AU} \left( \frac{M_*}{\text{M}_\odot} \right) \left( \frac{v_w}{100 \text{ km s}^{-1}} \right)^{-2}. \quad (15)$$

### 2.3. Central wind

We consider outflow rates  $\lesssim 10^{-8} \text{ M}_\odot \text{ yr}^{-1}$  that can be driven by the stellar wind (Decampli 1981), as well as higher outflow rates  $\lesssim 10^{-7} \text{ M}_\odot \text{ yr}^{-1}$  that can be driven by the interaction of the rotating magnetic field with the accreting disk (Shu et al. 2000; Konigl & Pudritz 2000). We do not consider the initial acceleration of the wind since it is expected to strike the disk surface after achieving terminal velocity. For simplicity, we assume a spherically symmetric wind with an isotropic distribution of density  $\rho_w$  and velocity  $v_w$ . In this case, in a reference frame centered on the star, the wind density can be written as

$$\rho_w = \frac{\dot{M}_w}{4\pi v_w r^2} \sim 10^{-17} \text{ g cm}^{-3} \left( \frac{\dot{M}_w}{10^{-8} \text{ M}_\odot \text{ yr}^{-1}} \right) \left( \frac{v_w}{200 \text{ km s}^{-1}} \right)^{-1} \left( \frac{r}{1 \text{ AU}} \right)^{-2}, \quad (16)$$

where  $r^2 \equiv R^2 + z^2$  and  $\dot{M}_w$  is the outflow mass loss rate per unit time.

Our model could easily be extended to also include collimated winds. We note that the assumption of spherical symmetry and isotropic distribution is required only in the small solid angle subtended by the disk. If the wind is substantially collimated, then the true wind mass loss rate is substantially higher than the  $\dot{M}_w$  used in our “spherically symmetric” models.

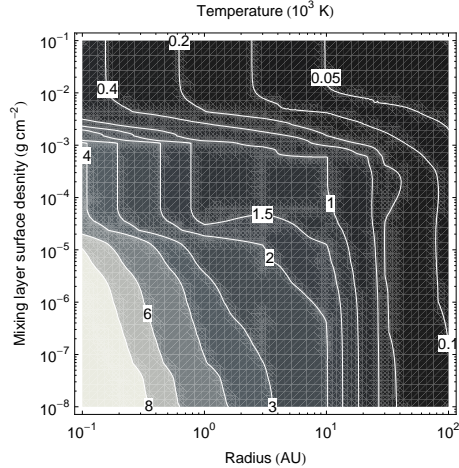


FIG. 3.— Contours of the gas temperature (in units of  $10^3$  K) in the mixing layer surface density-disk radius parameter space. This is the surface temperature of the disk just below the mixing layer.

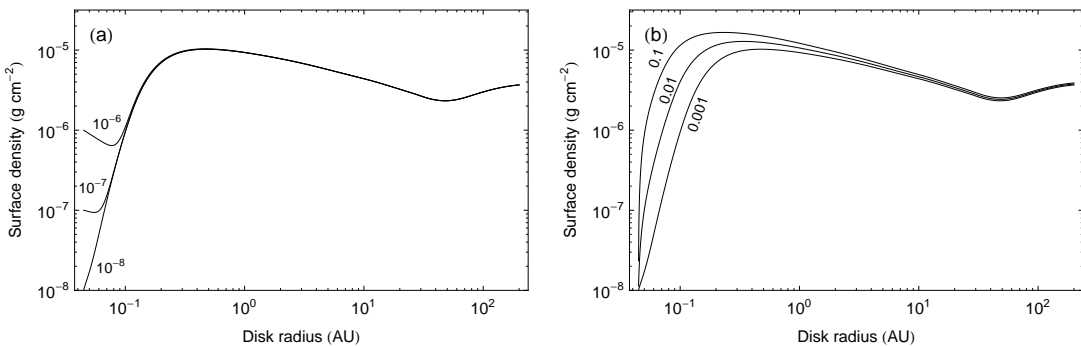


FIG. 4.— Mixing layer surface density as a function of disk radius for different boundary conditions and an entrainment efficiency  $\epsilon = 0.1$ . (a) Solutions for a wind incidence angle of  $0.001^\circ$  and different mixing layer surface densities at the inner boundary ( $10^{-6}$ ,  $10^{-7}$ , and  $10^{-8}$   $\text{g cm}^{-2}$ , as labeled on each line). (b) Solutions for a mixing layer surface density of  $10^{-8}$   $\text{g cm}^{-2}$  and different wind incidence angles at the inner boundary ( $0.001$ ,  $0.01$ , and  $0.1^\circ$ , as labeled on each line).

### 3. RESULTS

We find steady state solutions (i.e.  $\partial_t \Sigma_m = \partial_t \Sigma_m v_m = \partial_t \Sigma_m \Omega_m = 0$ ) of equations (3)-(5) with the boundary conditions  $\Sigma_m(R_{min}) = \Omega_m(R_{min}) = 0$  and  $\gamma(R_{min}, z_m(R_{min})) = \gamma_0$ , where  $\gamma_0$  is a small initial wind incidence angle at  $R_{min}$ . We assume a solar mass star, and a ballistic wind with  $v_w = 200$   $\text{km s}^{-1}$  and  $\dot{M}_w = 10^{-8} M_\odot \text{ yr}^{-1}$  in our fiducial model.

We use the detailed thermo-chemical disk model of Gorti & Hollenbach (2008) to separately calculate the gas temperature, the sound speed, and the gas density at the boundary between ambient disk and mixing layer. This model includes FUV and X-ray radiation, dust collisions, photo-reactions, and chemistry. For simplicity, we extrapolate calculations at specific disk radii (1, 3, 10, 30, and 100 AU) to calculate the gas temperature at different radii. Figure 3 shows contours of temperature in the disk radius-surface density parameter space. Here, surface density is measured from high  $z$  downward toward the disk midplane. The sharp transition at surface densities  $\sim 10^{-3}$   $\text{g cm}^{-2}$  is due to dust extinction of stellar photons, and the transition at  $\sim 10^{-5}$   $\text{g cm}^{-2}$  is caused by a complicated interplay of X-ray heating and ionization combined with [Ne II] and [Ar II] cooling. The transition at  $\sim 20$  AU is due to a relatively sudden inability of FUV and X-ray heating to maintain gas temperatures  $\gg 300$  K. Beyond this point [O I]  $63 \mu\text{m}$  cooling can maintain gas temperatures  $\lesssim 200$  K.

Figure 4 shows the mixing layer surface density for  $\epsilon = 0.1$ , a likely high efficiency, and different initial wind incidence angles and mixing layer surface densities at the inner boundary varying over several orders of magnitude. This figure illustrates that solutions at large radii ( $R \gtrsim 1$  AU) are insensitive to the exact inner boundary conditions used for a given value of  $\epsilon$ .

We summarize the main results for  $\epsilon = 0.1$  in Figure 5. Although the wind-disk mixing layer accumulates material from the wind and the underlying disk on the way out, surface density variations in the mixing layer become small (at  $R \gtrsim 1$  AU, see Figure 5a) due to the increasing surface area.

The wind-disk mixing layer is above the disk scale height (Figure 5b) because the small wind incidence angles (Figure 5c) result in correspondingly small wind ram pressures that can be balanced by the small disk pressure at large height. The disk pressure,  $P_d \equiv \rho_d c_s^2 (1 + \epsilon^2)$ , is larger than the normal wind pressure,  $P_w \equiv \rho_w v_w^2 \sin^2 \gamma$ , (Figure 5d) and thus

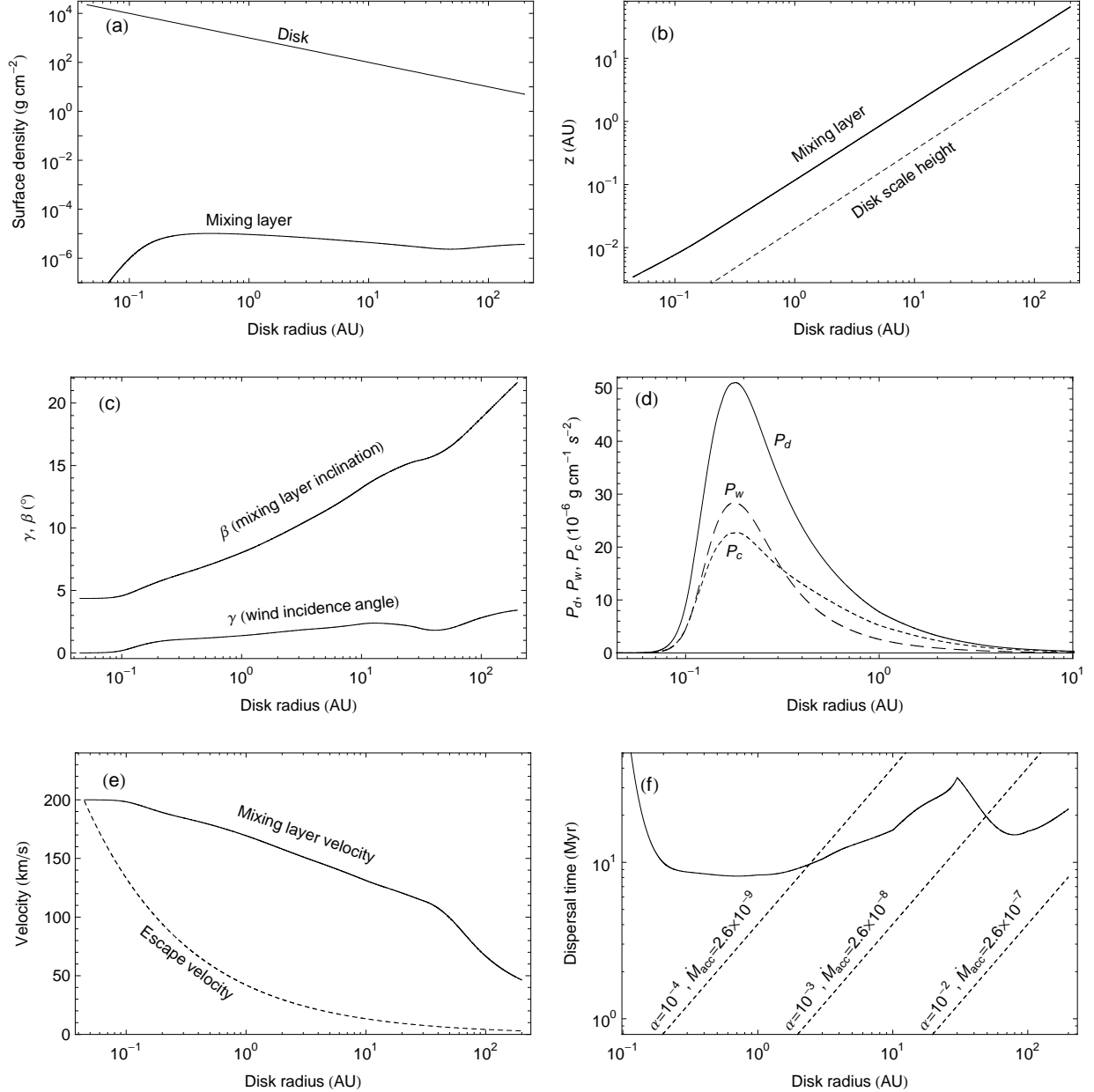


FIG. 5.— Mixing layer and disk parameters as a function of disk radius for an entrainment efficiency  $\epsilon = 0.1$ . The inner boundary conditions are a wind incidence angle of  $0.001^\circ$  and a zero mixing layer surface density. (a) Disk surface density,  $\Sigma_d$ , and mixing layer surface density,  $\Sigma_m$ , as labeled. (b) Mixing layer height (solid line) and disk scale height (dotted line). (c) Wind incidence angle,  $\gamma$ , and mixing layer inclination,  $\beta$ , as labeled. (d) Normal components of the disk pressure (solid line),  $P_d \equiv \rho_d c_s^2 (1 + \epsilon^2)$ , the wind pressure (dashed line),  $P_w \equiv \rho_w v_w^2 \sin^2 \gamma$ , and the curvature pressure term (dotted line),  $P_c \equiv \Sigma_m v_m^2 \cos \beta d\beta/dR$ . See equation (2) and Figure 2 for a description of this pressure terms. (e) Mixing layer velocity (solid line),  $v_m$ , and escape velocity (dotted line). (f) Disk dispersal time (solid line),  $\Sigma_d/\Sigma_{ws}$ , and viscous evolution time scales (dotted lines) for different  $\alpha$  viscosity values, as labeled.

the mixing layer surface flares outward with increasing radius (Figure 5c).

The mixing layer starts with roughly the same velocity as the wind at the inner boundary (Figure 5e) since the wind incidence angle is very small and very little disk mass has been entrained (Figure 5c); and slows down at larger radii as it accumulates mass from the disk (Figure 5e). Although the mixing layer velocity decreases with radius, it remains significantly higher than the escape velocity from the star.

We compare the wind dispersal time (eq. [9]) with the viscous evolution time scale (eq. [13]) for a range of accretion rates in Figure 5f. For our fiducial model ( $M_w = 10^{-8} M_\odot \text{ yr}^{-1}$ ,  $v_w = 200 \text{ km s}^{-1}$ , and  $\epsilon = 0.1$ ) and an accretion rate  $\sim 3 \times 10^{-8} M_\odot \text{ yr}^{-1}$ , viscous evolution is the dominant mechanism in the inner disk ( $\lesssim 50 \text{ AU}$ ) and wind stripping is the dominant mechanism in the outer disk in the absence of photoevaporation. We will explore the conditions under which wind stripping dominates the disk evolution in more detail below.

We derive an analytic expression for the dispersal time by assuming that the curvature term contribution to the

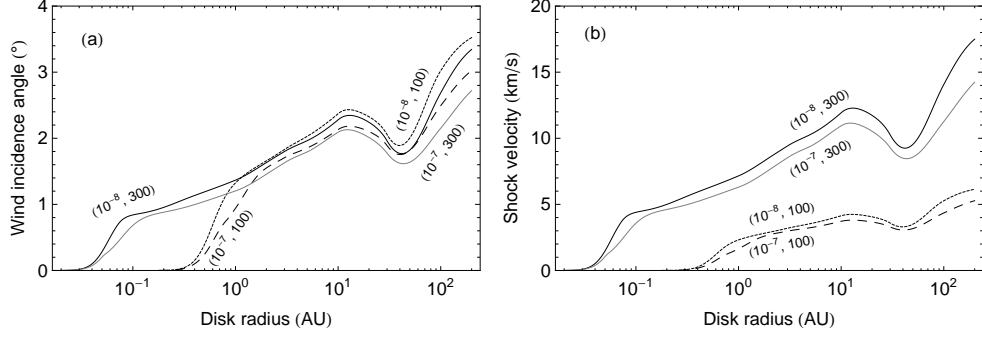


FIG. 6.— Wind incidence angle (a),  $\gamma$ , and shock velocity (b),  $v_s = v_w \sin \gamma$ , for an entrainment efficiency  $\epsilon = 0.1$ , stellar wind velocities in the range 100–300 km s<sup>-1</sup>, and wind outflow rates in the range  $10^{-7} - 10^{-8} M_\odot \text{ yr}^{-1}$ , as labeled. Changing the entrainment efficiency results in negligible variations.

normal pressure balance (eq. [2]) is similar to that of the stellar wind (Figure 5d). In this case, we can approximate the normal disk pressure as  $\rho_d c_s^2 (1 + \epsilon^2) \sim 2\rho_w v_w^2 \sin^2 \gamma$ , and the dispersal time (eq. [9]) as

$$t_{ws} \sim \frac{\pi \Sigma_d \cos \beta c_s R^2 (1 + \epsilon^2)}{\dot{M}_w v_w \epsilon \sin^2 \gamma}, \quad (17)$$

where we use equation (16) and  $r \sim R$ . We replace  $\beta \sim 10^\circ$  and  $\gamma \sim 2^\circ$  (Figure 5c) in equation (17) to obtain

$$t_{ws}(R) \sim 6 \text{ Myr} \left(\frac{\epsilon}{0.1}\right)^{-1} (1 + \epsilon^2) \left(\frac{\Sigma_0}{10^3 \text{ g cm}^{-2}}\right) \left(\frac{R}{\text{AU}}\right) \times \left(\frac{c_s}{4 \text{ km s}^{-1}}\right) \left(\frac{\dot{M}_w}{10^{-8} M_\odot \text{ yr}^{-1}}\right)^{-1} \times \left(\frac{v_w}{200 \text{ km s}^{-1}}\right)^{-1} \quad (18)$$

Note that the sound speed decreases with radius and mixing layer surface density (Figure 3). The decreasing sound speed means that  $Rc_s$  does not increase much with  $R$ , which leads to a fairly constant dispersal time as a function of  $R$  in this case where surface density drops with  $R^{-1}$ . Eq. [18] is in agreement with the estimate of Hollenbach et al. (2000). The highest dispersal rates (shortest dispersal times) correspond to the highest wind outflow rates and velocities, as expected. We can quantify the dispersing power of the wind with the parameter

$$\eta \equiv \left(\frac{\epsilon}{0.1}\right) \left(\frac{\dot{M}_w}{10^{-8} M_\odot \text{ yr}^{-1}}\right) \left(\frac{v_w}{200 \text{ km s}^{-1}}\right), \quad (19)$$

where we arbitrarily choose  $\eta = 1$  for our fiducial parameters.

Figures 6–8 compare results for models with different entrainment efficiencies, wind outflow rates, and wind velocities with our fiducial model ( $\epsilon = 0.1$ ,  $\dot{M}_w = 10^{-8} M_\odot \text{ yr}^{-1}$ ,  $v_w = 200 \text{ km s}^{-1}$ ). These results agree well with the analytic approximation given in Eq. (18).

We compare the wind incidence angles and the corresponding shock velocities for  $\epsilon = 0.1$ , wind outflow rates in the range  $10^{-7} - 10^{-8} M_\odot \text{ yr}^{-1}$ , and wind velocities in the range 100–300 km s<sup>-1</sup> in Figure 6. Variations due to changes in the entrainment efficiency are not significant. The wind incidence angle is not sensitive to  $\epsilon$ ,  $\dot{M}_w$ , or  $v_w$  since the mixing layer is located several disk scale heights above the midplane, where large changes in pressure (and mixing layer inclination) can be accommodated by small changes in the mixing layer height. The jogs at  $\sim 20 \text{ AU}$  are due to the rapid drop in gas temperature beyond this radius (Figure 3). We predict small wind incidence angles  $\gamma \lesssim 4^\circ$  and correspondingly small shock velocities (e.g.  $v_w \sin \gamma = 17 \text{ km s}^{-1}$  at 100 AU for  $\dot{M}_w = 10^{-8} M_\odot \text{ yr}^{-1}$  and  $v_w = 300 \text{ km s}^{-1}$ ).

We consider variations of the entrainment efficiency alone ( $\epsilon = 0.01 - 1$ ) in Figure 7. Only the mixing layer velocity and the dispersal time are shown since variations of the other quantities shown in Figure 5 are not significant. Increasing the entrainment efficiency decreases the mixing layer velocity and reduces the disk dispersal time, as expected since the mixing layer receives more mass from the underlying disk in this case. Although the mixing layer velocity decreases with radius as it entrains more mass from the disk, it is possible to maintain the maximum possible entrainment efficiency,  $\epsilon = 1$ , since the mixing layer velocity remains larger than the escape velocity at all radii.

Finally, we compare the dispersal mass flux rate and dispersal time due to wind stripping with those due to photoevaporation and the mass flux and characteristic time due to viscous evolution in Figure 8. Since the dispersal time depends on the particular disk surface density distribution assumed, the mass flux outflow rate (“dispersal rate”) is physically more meaningful. Hollenbach & Gorti (2009) show that EUV photons cannot penetrate the wind when the outflow rate is higher than  $\sim 10^{-9} M_\odot \text{ yr}^{-1}$ , while FUV and X-ray photons begin to penetrate once the outflow rate falls below  $\sim 10^{-7} M_\odot \text{ yr}^{-1}$ . Thus, we can ignore EUV photoevaporation for the high outflow rates ( $\gtrsim 10^{-9} M_\odot \text{ yr}^{-1}$ ) considered here. We compare the dispersal rates by wind stripping with those due to photoevaporation driven by FUV and X-ray heating (Gorti & Hollenbach 2009, Figure 4). We assume outflow rate/accretion rate ratios  $\chi \equiv \dot{M}_w / \dot{M}_{acc}$

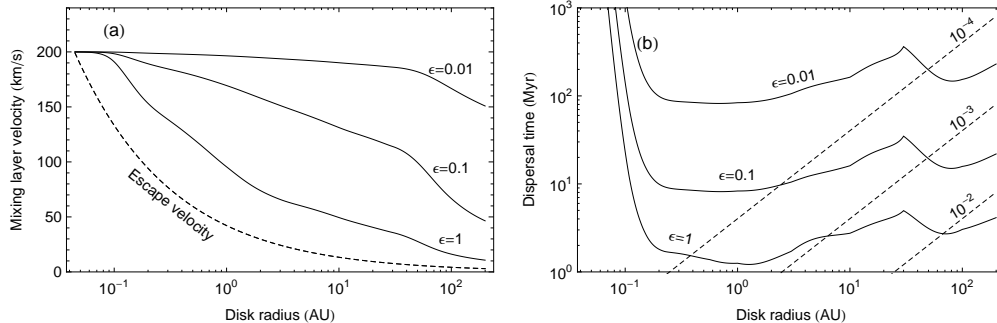


FIG. 7.— Mixing layer velocity (a) and disk dispersal time (b) as a function of disk radius for entrainment efficiencies in the range  $0.01 < \epsilon < 1$ , as labeled. The other wind parameters are standard ( $\dot{M}_w = 10^{-8} M_\odot \text{ yr}^{-1}$  and  $v_w = 200 \text{ km s}^{-1}$ ). The dotted lines in panel (b) give viscous evolution time scales for different  $\alpha$  viscosity parameters in the range  $10^{-4} < \alpha < 10^{-2}$ , as labeled.

in the range  $\sim 0.01 - 1$ , as inferred from observations (White & Hillenbrand 2004, Figure 16, excluding edge-on disks). It is useful to consider different accretion rate regimes (Figure 8):

- Low accretion rates ( $\lesssim 10^{-8} M_\odot \text{ yr}^{-1}$ , Figures 8a, b, c, and d). Viscous accretion is the dominant mechanism at most disk radii ( $\lesssim 150 \text{ AU}$ ), while photoevaporation is the dominant mechanism in the outermost regions ( $\gtrsim 150 \text{ AU}$ ). Wind stripping can be dominant at  $\sim 100 \text{ AU}$  if the wind outflow rate approaches the accretion rate ( $\chi \sim 1$ ). Once again, for  $\dot{M}_w \lesssim 10^{-9} M_\odot \text{ yr}^{-1}$ , EUV photons can penetrate the wind (Hollenbach & Gorti 2009) and EUV photoevaporation becomes dominant at  $\sim 1 \text{ AU}$  (Liffman 2003; Alexander et al. 2006a).
- Intermediate accretion rates ( $\sim 10^{-7} M_\odot \text{ yr}^{-1}$ , Figures 8e and f). Viscous accretion is the dominant mechanism in the inner disk ( $R \lesssim 60 \text{ AU}$ ), while photoevaporation is the dominant mechanism in the outer disk. Since the accretion rate also depends on the surface density (eq. [14]), we assume a surface density higher than our fiducial value ( $\Sigma_d = 5 \times 10^3 \text{ g cm}^{-2}$  at 1 AU) for intermediate and high accretion rates.
- High accretion rates ( $\gtrsim 10^{-6} M_\odot \text{ yr}^{-1}$ , Figures 8g and h). Viscous accretion is the dominant mechanism at all disk radii. In this case, although optical photons can reach and heat the disk, FUV and X-ray photons cannot penetrate the correspondingly high outflow rates (Hollenbach & Gorti 2009).

#### 4. SUMMARY AND CONCLUSIONS

We present a model for the dispersal of protoplanetary disks by winds from either the central star or the inner disk. These winds obliquely strike the flaring disk surface and strip away disk material by entraining it in an outward radial-moving flow at the wind-disk interface, located at the surface of normal pressure balance several disk scale heights above the mid-plane. We derive conservation equations for the mass, momentum, and angular momentum in the wind-disk interface.

The disk dispersal time scale depends on the velocity at which disk material is entrained into the mixing layer, which we quantify with an entrainment velocity  $\epsilon c_s$ , where  $c_s$  is the sound speed and  $\epsilon$  is an entrainment efficiency. The dispersal time decreases as  $(\epsilon v_w \dot{M}_w)^{-1}$  (see eq. [18]). For disk surface densities dropping as  $R^{-1}$ , the dispersal time is relatively independent of  $R$  (see Figs. 7 and 8 and Eq. [18]). We define a dimensionless parameter  $\eta \propto \epsilon v_w \dot{M}_w$  that is unity for our standard parameters  $\epsilon = 0.1$ ,  $v_w = 200 \text{ km s}^{-1}$ , and  $\dot{M}_w = 10^{-8} M_\odot \text{ yr}^{-1}$ . The dispersal time for  $\eta \sim 1$  (eq. [19]),  $t_{ws}(1 \text{ AU}) \sim 6(\Sigma_0/10^3 \text{ g cm}^{-2}) \text{ Myr}$ , is somewhat larger than typical protoplanetary (dust) disk evolutionary time scales ( $\sim 2 \text{ Myr}$ ) inferred from infrared observations (e.g. Haisch et al. 2001; Cieza et al. 2007). In fact, as discussed below, viscous evolution and photoevaporation likely dominate disk dispersal.

Figure 9 depicts the dominant physical mechanisms for different accretion rate regimes. For low accretion rates ( $\lesssim 10^{-8} M_\odot \text{ yr}^{-1}$ ), viscous accretion is the dominant mechanism at most disk radii ( $\lesssim 150 \text{ AU}$ ), while FUV and X-ray photoevaporation is the dominant mechanism in the outermost regions ( $\gtrsim 150 \text{ AU}$ ). In this case, wind stripping can be a dominant mechanism at  $\sim 100 \text{ AU}$  only if the wind outflow rates approach the accretion rates, which is rare. EUV photoevaporation becomes a dominant mechanism at  $\sim 1 \text{ AU}$  for low wind outflow rates ( $\lesssim 10^{-9} M_\odot \text{ yr}^{-1}$ ). For intermediate accretion rates ( $\sim 10^{-7} M_\odot \text{ yr}^{-1}$ ), viscous accretion is the dominant mechanism in the inner disk ( $\lesssim 60 \text{ AU}$ ), while FUV and X-ray photoevaporation is the dominant mechanism in the outer disk. For high accretion rates ( $\gtrsim 10^{-6} M_\odot \text{ yr}^{-1}$ ), viscous accretion dominates in the entire disk.

If wind stripping dominates viscous evolution, a gap may form if the inward accretion flow is less than the mass flux produced by wind entrainment at that radius, similar to the combined effects of viscous accretion and EUV photoevaporation (Clarke et al. 2001; Matsuyama et al. 2003; Alexander et al. 2006b). If the wind mass loss rate scales with the accretion rate, such as in X-wind models, then once a gap forms, accretion will rapidly decrease, the wind will turn off, and the gap will be refilled by viscous evolution of the outer disk. Time-dependent models which



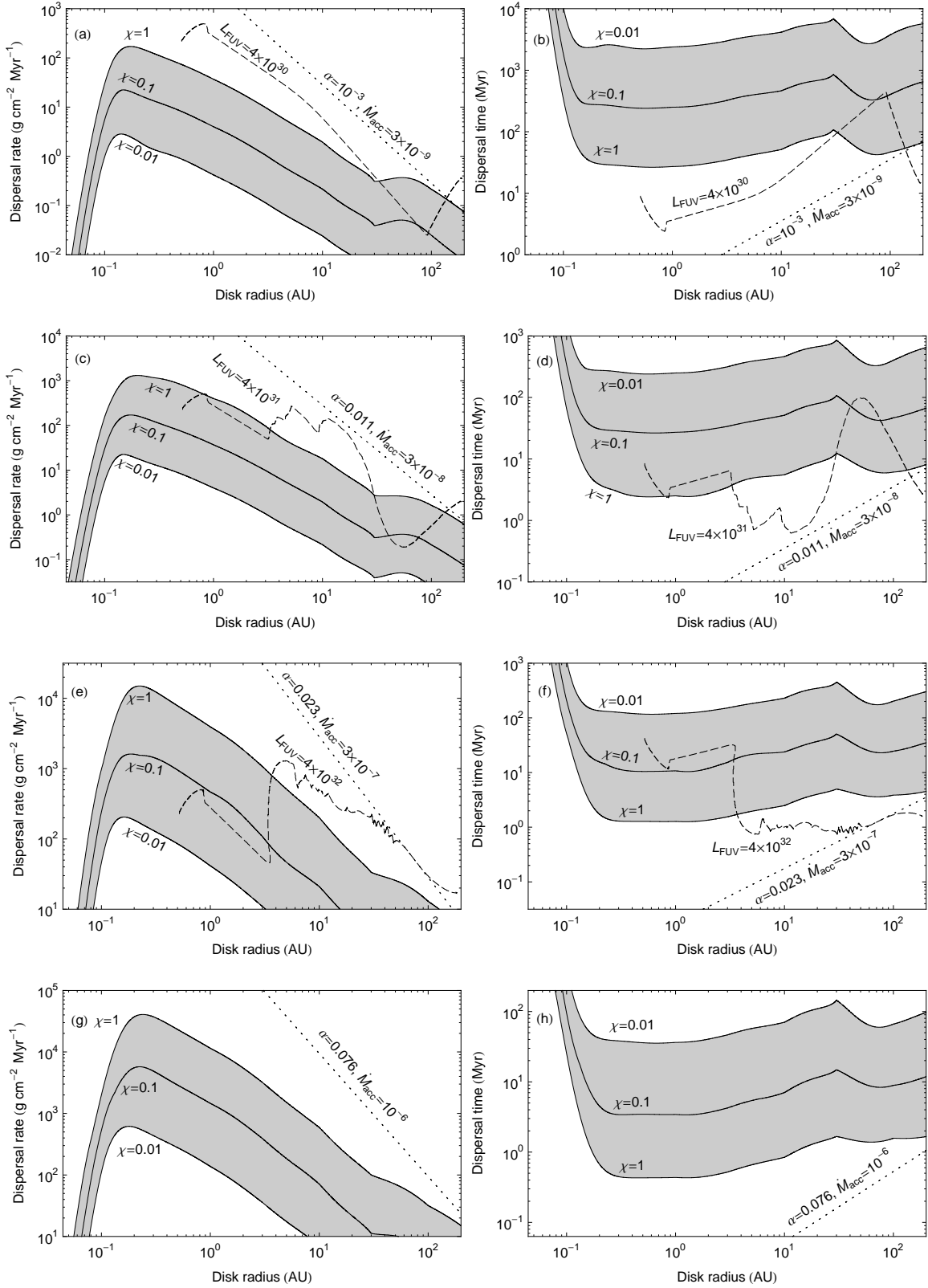


FIG. 8.— Dispersal rate and the corresponding dispersal time (solid lines) for  $\epsilon = 0.1$ ,  $v_w = 200 \text{ km s}^{-1}$ , and different outflow mass loss rate/accretion rate ratios  $\chi \equiv \dot{M}_w/\dot{M}_{acc}$ , as labeled. Dotted lines show the mass transport rate and the corresponding viscous evolution time scale due to accretion for accretion rates in the range  $3 \times 10^{-9} - 10^{-6} M_{\odot} \text{ yr}^{-1}$  (and the corresponding  $\alpha$  viscosity values using Eq. [14]), as labeled. Dashed lines show the photoevaporation dispersal rate and the corresponding dispersal time (from Figure 4 of Gorti & Hollenbach 2009) for the FUV luminosities,  $L_{FUV}$ , associated with the different accretion rates (Gorti & Hollenbach 2008), as labeled. We assume a surface density higher than our fiducial value ( $\Sigma_d = 5 \times 10^3 \text{ g cm}^{-2}$  at 1 AU) for correspondingly high accretion rates (e, f, g, and h).

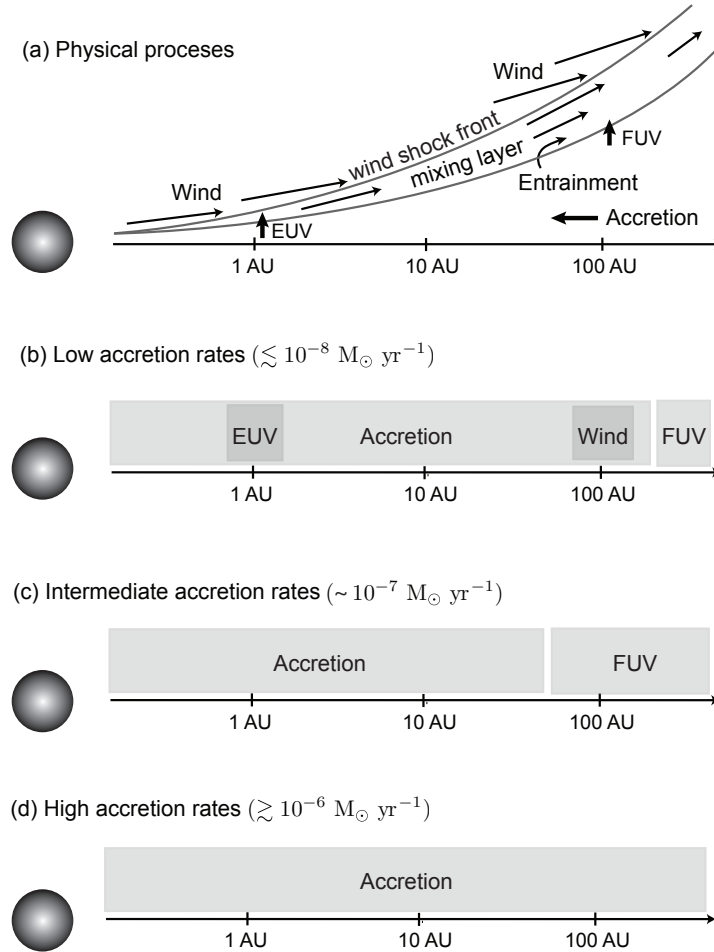


FIG. 9.— Schematic illustrations of the physical processes that dominate disk dispersal (a); and the accretion rate and disk radii regimes in which viscous accretion, EUV photoevaporation (EUV), FUV and X-ray photoevaporation (FUV), and wind stripping (wind) are dominant mechanisms (b, c, d). The central wind interacts directly with the disk at all radii since the mixing layer flares outward (Fig. 5c). In the mixing layer at a given radius, disk material mixes not only with the wind but also with the wind material already mixed with the disk gas at smaller radii. Note that in (b), EUV dominates at  $\sim 1$  AU only when the wind mass loss rate  $\lesssim 10^{-9} M_{\odot} \text{ yr}^{-1}$ .

include both the viscous evolution and mass loss by wind stripping are needed to explore this scenario. Once again, this requires wind outflow rates similar to the accretion rates (Figures 8a, c).

Hartmann & Raymond (1989) found that shock heating at the wind-disk interface can explain the observed forbidden line emission from large radii ( $\sim 50$ – $100$  AU). However, they predict shock velocities  $\sim 20$ – $30 \text{ km s}^{-1}$  (see their Figure 6), while we predict smaller shock velocities ( $\lesssim 17 \text{ km s}^{-1}$ , Figure 6b) and correspondingly small wind incidence angles ( $\lesssim 4^{\circ}$ , Figure 6a), even for wind velocities of  $300 \text{ km s}^{-1}$ , higher than the maximum value ( $200 \text{ km s}^{-1}$ ) assumed by Hartmann & Raymond (1989). The difference arises because Hartmann & Raymond (1989) assume that the tangential momentum of the mixing layer is given by the total accumulated tangential momentum of the wind while we solve for tangential momentum conservation [eq. (4)]. Note that mass input from the disk affects the tangential momentum of the mixing layer since it increases the mixing layer surface density. The observed [Ne II]  $12.8 \mu\text{m}$  forbidden line emission (e.g. Lahuis et al. 2007) may be explained by EUV or X-ray heating (Glassgold et al. 2007; Hollenbach & Gorti 2009), although the high [O I]  $6300 \text{ \AA}$  luminosities observed in some cases (Hartigan et al. 1995) defy explanation. The combination of EUV heating and ionization combined with turbulent mixing and heating in the wind-induced shear layer may provide the high gas temperature ( $\gtrsim 3000 \text{ K}$ ), high electron abundances, and high atomic O abundances needed to explain the [O I] luminosities. Further work is needed in this area.

We thank Uma Gorti for supplying us with prepublication results of her disk models that allowed us to estimate the temperature structure of the disk just below the shear layer created by the wind. This research was supported by the Miller Institute for Basic Research in Science, University of California, Berkeley; the Carnegie Institution of Washington; a Natural Sciences and Engineering Research Council of Canada grant; the NASA Astrophysical Theory program; and the NASA Astrobiology Institute.

APPENDIX  
CONSERVATION EQUATIONS

We consider normal pressure balance; and mass, momentum, and angular momentum conservation for a mixing layer annulus between  $R$  and  $R + \delta R$ , as shown in Figure 1. We denote the wind density, velocity, and incidence angle as  $\rho_w$ ,  $v_w$ , and  $\gamma$  respectively; the disk density and sound speed as  $\rho_d$  and  $c_s$  respectively, and the mixing layer surface density, velocity, and inclination as  $\Sigma_m$ ,  $v_m$ , and  $\beta$  respectively.

Force balance in the direction perpendicular to the surface of the annulus can be written as

$$2\pi R \delta s \rho_w v_w^2 \sin^2 \gamma + 2\pi R \Sigma_m v_m^2 \sin \delta\beta = 2\pi R \delta s \rho_d c_s^2 + 2\pi R \delta s \rho_d \epsilon^2 c_s^2. \quad (\text{A1})$$

On the left-hand-side (LHS) of equation (A1), the first and second terms correspond to the force associated with the normal momentum flux of the wind and the normal momentum flux through the inner boundary respectively (Figure 1). On the RHS of equation (A1), the first and second terms correspond to the thermal and ram pressure forces of the disk respectively. Replacing  $\delta s = \delta R / \cos \beta$  and taking the limits  $\delta R \rightarrow 0$  and  $\delta\beta \rightarrow 0$  in equation (A1) yields

$$\rho_w v_w^2 \sin^2 \gamma + \Sigma_m v_m^2 \cos \beta \frac{\partial \beta}{\partial R} = \rho_d c_s^2 (1 + \epsilon^2). \quad (\text{A2})$$

The second term on the LHS of equation (A2) is given by the product of the tangential momentum flux per unit length and time,  $\Sigma_m v_m^2$ , and the curvature of the mixing layer surface,  $\cos \beta d\beta/dR = d\beta/ds$ .

The mass and momentum in the direction tangent to the surface are  $2\pi R \delta s \Sigma_m$  and  $2\pi R \delta s \Sigma_m v_m$  respectively. The mass change per unit time is given by mass input from the wind and the disk, and mass transport through the annulus:

$$\frac{\partial}{\partial t} (2\pi R \Sigma_m \delta s) = 2\pi R \delta s \rho_w v_w \sin \gamma + 2\pi R \delta s \rho_d \epsilon c_s + 2\pi R \Sigma_m v_m - 2\pi R^+ \Sigma_m^+ v_m^+, \quad (\text{A3})$$

where we define  $R^+ \equiv R + \delta R$ ,  $\Sigma_m^+ = \Sigma_m(R^+, z(R^+), t)$ , and  $v_m^+ = v_m(R^+, z(R^+), t)$ . The last two terms on the RHS of equation (A3) correspond to the mass flux per unit time across the inner and outer boundaries of the annulus respectively. Replacing  $\delta s = \delta R / \cos \beta$  (Figure 1) and taking the limit  $\delta R \rightarrow 0$  in equation (A3) yields

$$\frac{\partial \Sigma_m}{\partial t} = \rho_w v_w \sin \gamma + \rho_d \epsilon c_s - \frac{\cos \beta}{R} \frac{\partial}{\partial R} (R \Sigma_m v_m). \quad (\text{A4})$$

Momentum conservation can be written as

$$\frac{\partial}{\partial t} (2\pi R \Sigma_m \delta s v_m) = 2\pi R \delta s \rho_w v_w^2 \sin \gamma \cos \gamma + 2\pi R \Sigma_m v_m^2 \cos \delta\beta - 2\pi R^+ \Sigma_m^+ v_m^{+2}, \quad (\text{A5})$$

where the last two terms on the RHS are the momentum flux per unit time across the inner and outer boundary of the annulus respectively. Replacing  $\delta s = \delta R / \cos \beta$  and taking the limits  $\delta\beta \rightarrow 0$  and  $\delta R \rightarrow 0$  in equation (A5) yields

$$\frac{\partial}{\partial t} (\Sigma_m v_m) = \rho_w v_w^2 \sin \gamma \cos \gamma - \frac{\cos \beta}{R} \frac{\partial}{\partial R} (R \Sigma_m v_m^2). \quad (\text{A6})$$

Assuming that the wind does not carry significant angular momentum, angular momentum conservation can be written as

$$\frac{\partial}{\partial t} (2\pi R \Sigma_m \delta s \Omega_m R^2) = 2\pi R \delta s \rho_d \epsilon c_s \Omega_k R^2 + 2\pi R \Sigma_m v_m \Omega_m R^2 - 2\pi R^+ \Sigma_m^+ v_m^+ \Omega_m^+ R^{+2}, \quad (\text{A7})$$

where  $\Omega_k = (GM/R^3)^{1/2}$  is the Keplerian angular velocity of the disk and  $\Omega_m$  is the angular velocity of the mixing layer. The angular velocity of the disk must be sub-Keplerian due to radial pressure support, by a factor  $\sim 1 - \mathcal{O}(H/R)^2$ , where  $H$  is the disk scale height. We ignore this effect since it is negligible for protoplanetary disks with  $(H/R)^2 \ll 1$ . The angular momentum loss due to the outward motion of the mixing layer [third and fourth terms on the RHS of equation (A7)] is partially compensated by the angular momentum input from the underlying disk [first term on the RHS of equation A7]. Once again, replacing  $\delta s = \delta R / \cos \beta$  and taking the limits  $\delta\beta \rightarrow 0$  and  $\delta R \rightarrow 0$  in equation (A7) yields

$$\frac{\partial}{\partial t} (\Sigma_m \Omega_m) = \rho_d \epsilon c_s \Omega - \frac{\cos \beta}{R^3} \frac{\partial}{\partial R} (R^3 \Sigma_m v_m \Omega_m). \quad (\text{A8})$$

REFERENCES

- |   |  |
|---|--|
| <p>Alexander, R., Clarke, C. J., &amp; Pringle, J. E. 2006a, Mon. Not. Roy. Astron. Soc., 369, 216</p> <p>Alexander, R. D., Clarke, C. J., &amp; Pringle, J. E. 2006b, Mon. Not. Roy. Astron. Soc., 369, 229</p> <p>Cabrit, S., Edwards, S., Strom, S. E., &amp; Strom, K. M. 1990, Astrophys. J., 354, 687</p> | <p>Cameron, A. G. W. 1973, Icarus, 18, 407</p> <p>Canto, J. 1980, A &amp; A, 86, 327</p> <p>Canto, J., &amp; Raga, A. C. 1991, Astrophys. J., 372, 646</p> |
|---|--|

- Cieza, L., Padgett, D. L., Stapelfeldt, K. R., Augereau, J.-C., Harvey, P., Evans, N. J., Merín, B., Koerner, D., Sargent, A., van Dishoeck, E. F., Allen, L. E., Blake, G. A., Brooke, T., Chapman, N., Huard, T., Lai, S.-P., Mundy, L., Myers, P. C., Spiesman, W., & Wahhaj, Z. 2007, *Astrophys. J.*, 667, 308
- Clarke, C. J., Gendrin, A., & Sotomayor, M. 2001, *Mon. Not. Roy. Astron. Soc.*, 328, 485
- D'Alessio, P., Canto, J., Calvet, N., & Lizano, S. 1998, *Astrophys. J.*, 500, 411
- Decampli, W. M. 1981, *Astrophys. J.*, 244, 124
- Elmegreen, B. G. 1978, *Moon and Planets*, 19, 261
- . 1979, *A & A*, 80, 77
- Glassgold, A. E., Najita, J. R., & Igea, J. 2007, *Astrophys. J.*, 656, 515
- Gorti, U., & Hollenbach, D. 2008, *Astrophys. J.*, 683, 287
- . 2009, *The Astrophysical Journal*, 690, 1539
- Haisch, K. E., Lada, E. A., & Lada, C. J. 2001, *Astrophys. J.*, 553, L153
- Handbury, M. J., & Williams, I. P. 1976, *The Observatory*, 96, 140
- Hartigan, P., Edwards, S., & Ghandour, L. 1995, *Astrophys. J.*, 452, 736
- Hartmann, L., Calvet, N., Gullbring, E., & D'Alessio, P. 1998, *Astrophys. J.*, 495, 385
- Hartmann, L., & Raymond, J. C. 1989, *Astrophys. J.*, 337, 903
- Hayes, W. D., & Probstein, R. F. 1966, *Hypersonic flow theory*, 2nd edn., Vol. 1 (Academic Press)
- Hollenbach, D., & Gorti, U. 2009, to be submitted to *ApJ*
- Hollenbach, D., Johnstone, D., Lizano, S., & Shu, F. H. 1994, *Astrophys. J.*, 428, 654
- Hollenbach, D., Yorke, H. W., & Johnstone, D. 2000, *Protostars and Planets IV*, 401
- Horedt, G. P. 1978, *A & A*, 64, 173
- Ida, S., & Lin, D. N. C. 2005, *Astrophys. J.*, 626, 1045
- Kenyon, S. J., & Hartmann, L. 1987, *Astrophys. J.*, 323, 714
- Koenigl, A., & Ruden, S. P. 1993, *Protostars and planets III*, 641
- Koenigl, A., & Pudritz, R. E. 2000, *Protostars and Planets IV*, 759
- Lahuis, F., van Dishoeck, E. F., Blake, G. A., Evans, N. J., Kessler-Silacci, J. E., & Pontoppidan, K. M. 2007, *Astrophys. J.*, 665, 492
- Liffman, K. 2003, *Publications of the Astronomical Society of Australia*, 20, 337
- Lynden-Bell, D., & Pringle, J. E. 1974, *Mon. Not. R. Astron. Soc.*, 168, 603
- Matsuyama, I., Johnstone, D., & Hartmann, L. 2003, *Astrophys. J.*, 582, 893
- Shakura, N. I., & Sunyaev, R. A. 1973, *A & A*, 24, 337
- Shu, F. H., Johnstone, D., & Hollenbach, D. 1993, *Icarus*, 106, 92
- Shu, F. H., Najita, J. R., Shang, H., & Li, Z.-Y. 2000, *Protostars and Planets IV*, 789
- White, R. J., & Hillenbrand, L. A. 2004, *Astrophys. J.*, 616, 998
- Wilkin, F. P., & Stahler, S. W. 1998, *Astrophys. J.*, 502, 661
- Yun, Y. S., Emori, H., & Nakazawa, K. 2007, *Earth Planets Space*, 59, 631